A physiologic rise in cytoplasmic calcium ion signal increases pannexin1 channel activity via a C-terminus phosphorylation by CaMKII

Ximena López[a], Nicolás Palacios-Prado[a,b], Juan Güiza[c], Rosalba Escamilla[a,b], Paola Fernández[b], José L. Vega[c], Maximiliano Rojas[d], Valeria Marquez-Miranda[b,e], Eduardo Chamorro[f], Ana M. Cárdenas[b], María Constanza Maldifassi[b], Agustín D. Martínez[b], Yorley Duarte[b,d], Fernando D. González-Nilo[b,d,1], and Juan C. Sáez[a,b,1]

[a]Departamento de Fisiología, Pontificia Universidad Católica de Chile, 6513677 Santiago de Chile, Chile; [b]Instituto de Neurociencias, Centro Interdisciplinario de Neurociencias de Valparaíso, Facultad de Ciencias, Universidad de Valparaíso, 2381850 Valparaíso, Chile; [c]Laboratorio GaPaL, Instituto Antofagasta, Universidad de Antofagasta, 1270300 Antofagasta, Chile; [d]Center for Bioinformatics and Integrative Biology, Facultad de Ciencias de la Vida, Universidad Andrés Bello, 8370146 Santiago, Chile; [e]Centro de Nanotecnología Aplicada, Facultad de Ciencias, Universidad Mayor, Santiago 8580745, Chile; and [f]Departamento de Ciencias Químicas, Facultad de Ciencias Exactas, Universidad Andrés Bello, 8370146 Santiago, Chile

This contribution is part of the special series of Inaugural Articles by members of the National Academy of Sciences elected in 2019.

Contributed by Juan C. Sáez, June 15, 2021 (sent for review May 14, 2021; reviewed by Jean Jiang and Alberto E. Pereda)

Pannexin1 (Panx1) channels are ubiquitously expressed in vertebrate cells and are widely accepted as adenosine triphosphate (ATP)-releasing membrane channels. Activation of Panx1 has been associated with phosphorylation in a specific tyrosine residue or cleavage of its C-terminal domains. In the present work, we identified a residue (S394) as a putative phosphorylation site by Ca^{2+}/calmodulin-dependent kinase II (CaMKII). In HeLa cells transfected with rat Panx1 (rPanx1), membrane stretch (MS)-induced activation—measured by changes in DAPI uptake rate—was drastically reduced by either knockdown of Piezo1 or pharmacological inhibition of calmodulin or CaMKII. By site-directed mutagenesis we generated rPanx1S394A-EGFP (enhanced green fluorescent protein), which lost its sensitivity to MS, and rPanx1S394D-EGFP, mimicking phosphorylation, which shows high DAPI uptake rate without MS stimulation or cleavage of the C terminus. Using whole-cell patch-clamp and outside-out excised patch configurations, we found that rPanx1-EGFP and rPanx1S394D-EGFP channels showed current at all voltages between ±100 mV, similar single channel currents with outward rectification, and unitary conductance (~30 to 70 pS). However, using cell-attached configuration we found that rPanx1S394D-EGFP channels show increased spontaneous unitary events independent of MS stimulation. In silico studies revealed that phosphorylation of S394 caused conformational changes in the selectivity filter and increased the average volume of lateral tunnels, allowing ATP to be released via these conduits and DAPI uptake directly from the channel mouth to the cytoplasmic space. These results could explain one possible mechanism for activation of rPanx1 upon increase in cytoplasmic Ca^{2+} signal elicited by diverse physiological conditions in which the C-terminal domain is not cleaved.

pannexin1 channel | permeability | phosphorylation | site-directed mutagenesis | unitary events

Pannexin1 (Panx1) is a glycoprotein ubiquitously expressed by vertebrate cells (1, 2). It oligomerizes as a heptamer forming a nonjunctional membrane channel with distinct open conformations and multimodal activation (3–5). Without stimulation, Panx1 channels adopt a conformation that appears to be sensitive to changes in membrane potential (strong depolarization) and selective for chloride ions (6, 7). However, Panx1 channels undergo conformational changes upon different types of stimulation, e.g., low oxygen tension, high extracellular K^+ concentration ($[K^+]_o$), membrane stretch (MS), different types of receptor activation, and elevated cytoplasmic free Ca^{2+} concentration $[Ca^{2+}]_i$, affecting the probability of dwelling in several distinct channel states with unique conductance and/or permeability properties (8–14). After stimulation, Panx1 channels are "activated" and allow the passage of small molecules (i.e., glucose and adenosine triphosphate [ATP]), monovalent cations (15), and small cationic molecules such as DAPI (16).

The understanding about electrophysiological and permeability properties of Panx1 channels has changed over the years (3, 4). The current view of the Panx1 channel under normal conditions is that it behaves as a constitutively active and selective chloride channel, with outward rectifying properties and no (or very low) permeability to ATP or cationic dyes (6, 17–19). This channel conformation exhibits unitary conductance from ~15 pS at negative potentials to ~90 pS at positive potentials (unitary conductance varies depending on ion concentration and composition of recording solutions and cell type). Another consensus is that Panx1 channels need to be "activated" to become permeable to ATP and cationic dyes. However, it is a matter of debate whether this "activation" requires a big conformational change to allow ATP passage (3, 20).

Under various conditions including high $[K^+]_o$, oxygen–glucose deprivation, hypertonic conditions, or exposure to caffeine,

Significance

This work shows that rat and human pannexin1 channels are not intrinsically sensitive to membrane stretch and their activation, previously associated with a physiologic increase in cytoplasmic Ca^{2+} concentration, results from phosphorylation via CaMKII in the amino acid residue S394 located in the C terminus of pannexin1. This posttranslational modification does not significantly affect the unitary conductance of the channel but increases the permeability of lateral tunnels to adenosine triphosphate (ATP) and permits the influx of positively charged molecules, such as DAPI, via the external vestibule to the cytoplasm. This activation mechanism might explain the ATP release via pannexin1 channels in diverse cell types under numerous physiologic conditions.

Author contributions: X.L., N.P.-P., R.E., F.D.G.-N., and J.C.S. designed research; X.L., N.P.-P., J.G., R.E., P.F., M.R., V.M.-M., E.C., M.C.M., and Y.D. performed research; A.D.M. contributed new reagents/analytic tools; X.L., N.P.-P., J.G., R.E., P.F., M.R., V.M.-M., E.C., M.C.M., Y.D., F.D.G.-N., and J.C.S. analyzed data; and X.L., N.P.-P., J.G., R.E., J.L.V., V.M.-M., E.C., A.M.C., M.C.M., A.D.M., Y.D., F.D.G.-N., and J.C.S. wrote the paper.

Reviewers: J.J., University of San Antonio; and A.E.P., Albert Einstein College of Medicine.

The authors declare no competing interest.

[1]To whom correspondence may be addressed. Email: fernando.gonzalez@unab.cl or juancarlos.saez@uv.cl.

This article contains supporting information online at https://www.pnas.org/lookup/suppl/doi:10.1073/pnas.2108967118/-/DCSupplemental.

Published July 23, 2021.

a nonrectifying large-conductance (>300 pS) ATP-releasing channel identified as a Panx1 channel has been reported (8, 9, 21, 22). Nonetheless, removal of the C terminus and activation of α1D-adrenoreceptors also "activate" Panx1 channels and induce ATP release and cationic dye uptake without a mayor change in single-channel conductance and rectifying properties (20). A rise in $[Ca^{2+}]_i$ is a converging point of numerous cellular stimuli. Notably, a graded increase in Panx1 channel activity with increasing $[Ca^{2+}]_i$ has been demonstrated in *Xenopus* oocytes (20), but the molecular mechanism remains largely unknown. In diverse cell types, rises in $[Ca^{2+}]_i$ have been related to purinergic signaling induced by extracellular ATP, which activates metabotropic or ionotropic P2 receptors (8, 23–25). A putative stretch sensitivity of Panx1 channels has been challenged since they were not activated by swelling in *Xenopus* oocytes (26). Nonetheless, the participation of a well-accepted stretch-activated membrane channel, such as Piezo1, might explain the MS-induced rise in $[Ca^{2+}]_i$ and its subsequent Panx1 channel activation. At least two examples favor this hypothesis. In urothelial cell cultures Piezo1 is involved in stretch-evoked Ca^{2+} influx and ATP release via Panx1 channels (27), whereas in endothelial cells Piezo1 controls blood pressure by mediating flow-induced ATP release via Panx1 channels (28).

Here, we describe a phosphorylation-dependent mechanism activated by a transient and localized rise in cytosolic Ca^{2+} signal which involves upstream activation of Piezo1 channels, and downstream activation of calmodulin and CaMKII, resulting in phosphorylation of rat Panx1 (rPanx1) and conformational changes of lateral tunnels and selectivity filter. The outcome of these events is elevated Panx1 channel activity and permeability to DAPI, without significant modifications in single-channel conductance, outward rectifying properties, or length of the C-terminal end of Panx1. These findings indicate that rPanx1 channels are not directly sensitive to MS, and their permeability properties are modulated by phosphorylation-dependent signaling cascades under physiological conditions.

Results

The MS-Induced Increase in rPanx1 Channel Activity Depends on the Activation of the Piezo1 Channel and Submembrane Increase in Ca^{2+} Signal. Since MS has been shown to increase the activity of rPanx1-EGFP (enhanced green fluorescent protein) channels (29, 30) and this response can be mediated by stretch-activated channels, we evaluated changes in MS-induced dye-uptake rate in HeLa rPanx1-EGFP transfectants under pharmacological blockade of different know stretch-sensitive channels, such as MS-activated channels (MSCs) or Piezo1 (27, 28). In DAPI uptake experiments we found that the MS-induced DAPI uptake rate in HeLa rPanx1-EGFP preincubated for 30 min with 200 μM La^{3+}, a blocker of various Ca^{2+}-permeable channels, including MSCs (31), was reduced to baseline values (*SI Appendix*, Fig. S1*A*). However, the MS-induced DAPI uptake rate was not altered by acute application of La^{3+} (*SI Appendix*, Fig. S1*B*). Since MSCs are permeable to Mg^{2+} and Ca^{2+} (32, 33) we evaluated whether the increase in rPanx1-EGFP channel activity induced by MS depends on these extracellular cations. In the absence of Ca^{2+} or both cations the MS-induced DAPI uptake rate was similar to baseline, while in the absence of extracellular Mg^{2+} it was similar to that recorded in cells bathed with complete Krebs medium (*SI Appendix*, Fig. S1*C*). Since rPanx1 channels are not permeable to Ca^{2+} (29), the above results suggest that HeLa cells express MS-sensitive channels that allow the entry of extracellular Ca^{2+} that subsequently activates rPanx1-EGFP channels. Therefore, we studied whether pharmacological activation of Piezo1 with the agonist Yoda1 (34) affects $[Ca^{2+}]_i$ in HeLa cells loaded with the ratiometric Ca^{2+} indicator FURA-2 (F340/F380 emissions). Yoda1 (25 μM) was found to increase $[Ca^{2+}]_i$ (*SI Appendix*, Fig. S2 *A* and *B*) and the DAPI uptake rate in a concentration-dependent manner (*SI Appendix*, Fig. S2*C*). Moreover, treatment with 10 μM carbenoxolone (CBX) drastically reduced the dye uptake induced by Yoda1 to values similar to those obtained under control conditions (*SI Appendix*, Fig. S2*D*), suggesting that Yoda1 induces an increase in rPanx1-EGFP channel activity. To confirm this possibility, MS-induced DAPI uptake was evaluated in cells transfected with a morpholino against Piezo1 at two different concentrations. After MS stimulation, DAPI uptake of these cells was reduced to ∼50% with respect to cells transfected with control morpholino (*SI Appendix*, Fig. S2*E*). We measured submembrane Ca^{2+} signals in HeLa cells transfected with a genetically encoded Ca^{2+} indicator protein, GCAMP3, that includes a membrane-tethering domain using a total internal reflection fluorescence (TIRF) microscope. Under these conditions we found that MS-induced stimulation produced a fast (<10-s rise) and transient (<1-min total duration) Ca^{2+} increase in submembrane areas (*SI Appendix*, Fig. S3).

MS-Induced rPanx1-EGFP Channel Activation Requires Active CaMKII. Since rPanx1 does not present Ca^{2+}-binding domains we have previously proposed a possible involvement of an indirect mechanism such as phosphorylation by a Ca^{2+}-dependent protein kinase (25). To evaluate this possibility, HeLa cells transfected with rPanx1-EGFP were preincubated (30 min) with W7, a cell-permeable calmodulin antagonist. Under these conditions the MS-induced DAPI uptake

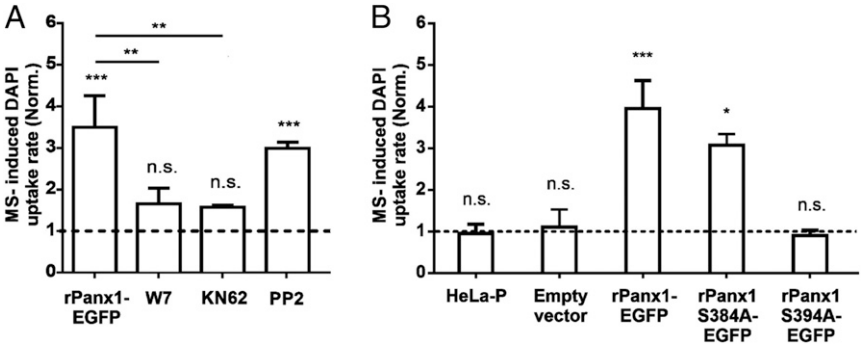

Fig. 1. The activation of Panx1 channels induced by MS in HeLa rPanx1 cells depends on the Ca^{2+}–calmodulin complex, CaMKII kinase activity, and residue S394. (*A*) DAPI uptake rate normalized with respect to baseline uptake in HeLa rPanx1-EGFP cells pretreated or not for 30 min with 100 μM W7, 10 μM KN62, or 10 μM PP2, subjected to MS. The DAPI uptake assays were performed in the presence of the above-mentioned compounds. Each value corresponds to the mean ± SE of a total of three to four independent experiments. (*B*) To test the involvement of putative phosphorylation site by CaMKII, DAPI uptake rate was normalized with respect to baseline uptake of nontransfected HeLa-P cells subjected to MS, or transfected with the pRK5 vector with or without the following inserts: rPanx1-EGFP, rPanx1S384A-EGFP, or rPanx1S394A-EGFP. The dye uptake assay was performed 24 h posttransfection. Each value corresponds to the mean ± SE of a total of three to eight independent experiments. $^{**}P < 0.005$; $^{***}P < 0.001$; n.s., nonsignificant.

rate of HeLa rPanx1-EGFP cells was ∼1.9 times lower than that measured in the absence of W7 (Fig. 1*A*). Since the Ca^{2+}–calmodulin complex can activate CaMKII (35), we then evaluated whether the activity of this protein kinase was required. HeLa rPanx1-EGFP cells were preincubated with the CaMKII inhibitor KN62 (10 μM) for 30 min. The MS-induced DAPI uptake rate in HeLa rPanx1 cells was ∼1.9 times lower in the presence of KN62 compared to nontreated cells (Fig. 1*A*), indicating that the MS-induced activation of rPanx1-EGFP channels depends on the Ca^{2+}–calmodulin complex and CaMKII kinase activity.

We also studied whether the increase in MS-induced activity of rPanx1 channels depends on the Src family kinases (SFKs), which have been shown to increase the activity of Panx1 channels through phosphorylation of tyrosine residues 198 and 308 (36, 37). In HeLa rPanx1 cells pretreated for 30 min with PP2, an inhibitor of SFKs, the MS-induced DAPI uptake rate showed no significant difference from nontreated cells (Fig. 1*A*), suggesting that SFKs do not participate in the MS-induced response.

Serine 394 Participates in the MS-Induced Activity of rPanx1 Channels. Since activation of rPanx1-EGFP channels induced by MS depends on the Ca^{2+}-calmodulin complex and CaMKII activity, we tested whether CaMKII could phosphorylate rPanx1 and thus modulate channel permeability. To this end, we searched for potential phosphorylation sites in rPanx1 by CaMKII (see *Materials and Methods*) and found two putative phosphorylation sites; the Plotter bioinformatics tool predicts that they are located at the C-terminal end: S384 and S394. Then, we performed individual alanine substitutions of these two residues in rPanx1-EGFP, so that they could not be phosphorylated.

MS-induced DAPI uptake rate was evaluated in nontransfected parental HeLa cells (HeLa-P), cells transfected (24 h posttransfection) with the pRK5 vector that contains only the EGFP insert (empty vector) or containing rPanx1-EGFP or the different rPanx1 mutants. Cells nontransfected or transfected with the empty vector were insensitive to MS (Fig. 1*B*). However, cells transfected with the construct containing rPanx1-EGFP were sensitive to MS, obtaining an increase in the DAPI uptake rate approximately four times greater than baseline (Fig. 1*B*). While the DAPI uptake rate of the S384A mutant was comparable to that obtained in cells transfected with rPanx1-EGFP, the DAPI uptake rate in the S394A mutant was comparable to nontransfected cells or cells transfected with the empty vector (Fig. 1*B*).

To confirm that S394 is involved in the MS-dependent activation of rPanx1-EGFP channels, this residue was substituted by aspartate to simulate a permanent phosphorylated residue. In these experiments, we evaluated DAPI uptake rate in the absence of MS stimulation at 6, 12, and 24 h posttransfection. Since the highest DAPI uptake activity of rPanx1S394D-EGFP channels was found at 12 h, we decided to perform the rest of the experiments at 12 h posttransfection. At this time, a robust vesicular pattern of EGFP fluorescence was observed in HeLa cells expressing rPanx1S394D-EGFP, suggesting that under these conditions the hyperactivity of rPanx1S394D-EGFP channels favors its internalization (Fig. 2*A*). It has been shown that activated Panx1 channels interact with P2 receptors, which is followed by down-regulation and internalization (38). However, inhibition of P2 receptors prevents the vesicular internalization (38). Consequently, to prevent internalization to endosomal compartments, HeLa cells expressing rPanx1S394D-EGFP were incubated during this 12-h period with 100 μM suramin, a blocker of P2 receptors (39). In HeLa rPanx1-EGFP, with or without suramin, the vesicular distribution of EGFP-fused rPanx1 was minimal. In HeLa rPanx1S394D-EGFP treated with suramin the fluorescence pattern distribution of EGFP was similar to that of cells transfected with rPanx1-EGFP (Fig. 2*A*).

Subsequently, differences in DAPI uptake rate were evaluated in HeLa cells transfected with rPanx1-EGFP or rPanx1S394D-EGFP mutant in the absence of MS stimulation. The DAPI uptake rate of HeLa rPanx1-EGFP treated with 100 μM suramin was similar to that of untreated cells (Fig. 2*B*). Similar results were obtained in HeLa rPanx1-EGFP treated with 100 μM suramin and pretreated for 30 min with 200 μM of the rPanx1 mimetic peptide ^{10}Panx1 (Fig. 2*B*), a selective inhibitor of Panx1 channels (10). In the HeLa rPanx1S394D-EGFP mutant treated with 100 μM suramin the dye uptake rate was approximately five times higher than that of cells not treated with suramin. This high uptake may be explained by a reduction in internalization together with a constitutive high activity of the rPanx1S394D-EGFP channels. The latter was tested by preincubating suramin-treated cells for 30 min with 200 μM ^{10}Panx1, and we found that the DAPI uptake rate was similar to the condition without suramin treatment (Fig. 2 *B* and *C*). The uptake rates for HeLa-P (0.03), HeLa rPanx1-EGFP (0.11), rPanx1-EGFP + suramin (0.14), rPanx1S394D-EGFP (0.08), or rPanx1S394D-EGFP + suramine (0.62) show significant differences only in the case of the S394D mutant treated with suramin with respect to the other groups. Thus, S394 is likely to participate in the increase of Panx1 channel activity induced by MS. Since human Panx1 (hPanx1) does not present the S394 site, we tested whether this natural variant can form MS-sensitive channels. Indeed, HeLa cells transfected with hPanx1 showed a small increase in DAPI uptake upon MS, which was completely prevented by cyclosporin A, a calcineurin blocker (*SI Appendix*, Fig. S4), which presumably prevents dephosphorylation of protein kinase A (PKA)-phosphorylated residues present in both rPanx1 and hPanx1. PKA-dependent phosphorylation was recently shown to prevent activation of the rPanx1 channel (40).

It has been demonstrated that increases in $[Ca^{2+}]_i$ lead to activation of proteases that can cleave the C-terminal domain of hPanx1, causing ATP release (12, 20). However, in our experimental conditions we did not notice an evident reduction in confocal fluorescence intensity of rPanx1-EGFP or a reduction either in the amount of rPanx1-EGFP or in the appearance of a C-terminal peptide evaluated by Western blot analysis in total protein samples of HeLa rPanx1-EGFP cells subjected to MS (*SI Appendix*, Fig. S5), suggesting that under our experimental conditions the C terminus of rPanx1 is not cleaved.

rPanx1S394D-EGFP Forms Channels with More Spontaneous Unitary Events with Conductance Similar to rPanx1-EGFP Channels. To study the differences in spontaneous unitary events and conductance between HeLa-P and HeLa cells expressing rPanx1-EGFP and rPanx1S394D-EGFP channels, we used the patch-clamp technique in cell-attached, whole-cell, and outside-out configurations. To induce current changes we used a stepwise voltage protocol from −100 to +100 mV applied via 20-mV increments and of 2.5 s in duration (*SI Appendix*, Fig. S6). HeLa-P cells show low current levels in all three configurations and did not respond to changes in membrane potential (V_m) (*SI Appendix*, Fig. S6 *A* and *D*). In contrast, HeLa cells expressing rPanx1-EGFP or rPanx1S394D-EGFP (both pretreated with 100 μM suramin) showed changes in macroscopic currents (whole-cell configuration) and in excised patches (outside-out configuration). At the beginning of the experiments, average total currents measured at −20 mV were 2.4 ± 0.35 nA or 1.1 ± 0.25 nA for HeLa cells expressing rPanx1-EGFP or rPanx1S394D-EGFP, respectively (*SI Appendix*, Fig. S7*A*). Interestingly, after a few minutes (∼2 min) of establishing whole-cell configuration the average total current in HeLa cells expressing rPanx1-EGFP increased 1.47-fold, while HeLa cells expressing rPanx1S394D-EGFP did not show significant differences (*SI Appendix*, Fig. S7*A*). Instantaneous currents (measured at the beginning of each voltage step) in rPanx1-EGFP–expressing cells show a previously described outward rectifying behavior of Panx1 channels (*SI Appendix*, Fig. S6 *B* and *E*). However, steady-state currents (measured at the end of each voltage step) show some decrease at high depolarizing V_ms. The instantaneous current–voltage relationships were similar between rPanx1-EGFP– and

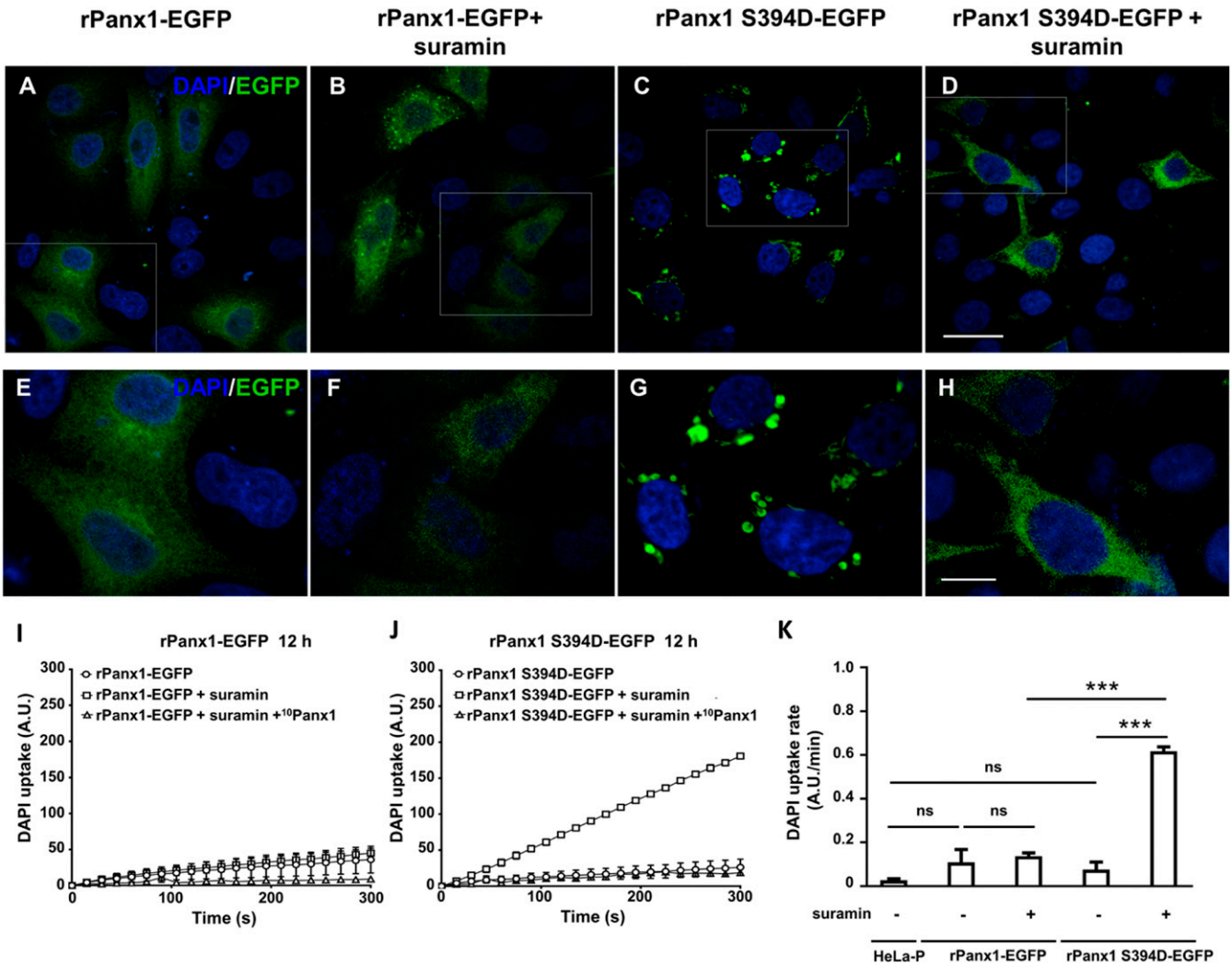

Fig. 2. Distribution of rPanx1-EGFP and rPanx1S394D-EGFP with and without pretreatment with suramin. (*A–H*). Representative confocal images of HeLa cells transiently transfected for 12 h with the complementary DNA of rPanx1-EGFP or rPanx1S394D-EGFP, treated or not with 100 μM suramin during the entire transfection period. *A–D* show a general view of each condition (scale bar: 25 μm), and *E–H* show a magnification of the white boxes marked in the images at the top (scale bar: 10 μm). (*I* and *J*) Representative DAPI uptake for HeLa cells transfected with rPanx1-EGFP (*I*) or with rPanx1S394D-EGFP (*J*), with or without pretreatment for 12 h with 100 μM suramin and for 30 min with 200 μM ^{10}Panx1. (*K*) Average DAPI uptake rate in HeLa-P, HeLa cells transfected with rPanx1-EGFP with and without 12-h pretreatment with 100 μM suramin, and HeLa transfected with rPanx1S394D-EGFP with and without 12-h pretreatment with 100 μM suramin. Dye uptake assays were performed 12 h posttransfection. Each value corresponds to the mean ± SE of a total of three independent experiments. ***$P < 0.001$; ns, nonsignificant.

rPanx1S394D-EGFP–expressing cells. Nonetheless, the sensitivity to high depolarizing V_ms seems reduced in rPanx1S394D-EGFP mutants (*SI Appendix*, Fig. S6 *C* and *F*).

To compare in more detail the difference between rPanx1-EGFP and rPanx1S394D-EGFP channels, we measured single-channel conductance at different V_ms in outside-out patches (Fig. 3). Both channels showed outward rectification at the single-channel level, with conductance of ∼30 pS at −80 mV to ∼70 pS at +80 mV (Fig. 3 *C–F*). However, spontaneous unitary events of rPanx1S394D-EGFP channels were normally detected at the cell-attached configuration while rPanx1-EGFP were silent (Fig. 3 *A* and *B* and *SI Appendix*, Fig. S7 *B* and *C*), even though the total current measured in rPanx1-EGFP–expressing cells during whole-cell configuration was more than double that measured in rPanx1S394D-EGFP. The outward rectifying behavior of rPanx1S394D-EGFP channels was also detected in the cell-attached configuration at the single channel level, and these active channels are mainly open at ±20 mV (*SI Appendix*, Fig. S7 *B* and *C*). In summary, S394D mutation induces spontaneous unitary events of rPanx1 channel measured in the cell-attached configuration, while rPanx1 remains silent. These differences are accompanied by a slight change in V_m sensitivity at high positive potentials. However, rPanx1-EGFP and rPanx1S394D-EGFP channels show no significant differences in single-channel conductance and outward rectifying properties.

Role of Arginine–Tryptophan Interaction in the Selectivity Filter. The rPanx1 channel selectivity filter presents a ring of seven pairs of arginine (R) and tryptophan (W) residues, stabilized through a cation–π interaction in a T-shaped configuration (*SI Appendix*, Fig. S8*A*). Interestingly, Cl^- crosses the selectivity filter by establishing contact with the aromatic rings of the W residues through an anion–π interaction, while the R residues, in a "second row," contribute with an electropositive potential that makes this particular selectivity filter allow the translocation of Cl^- through the pore. In addition, the R ring generates a high density of positive charges in a small space, generating a high electropositive density in a dielectric medium that should be relatively low due to the interaction between arginine and tryptophan residues. This electrostatic

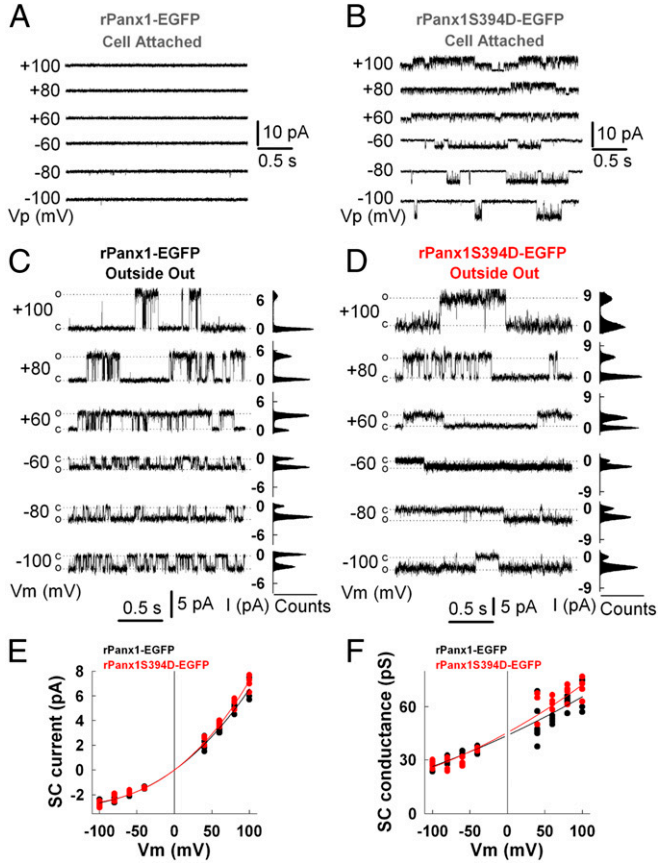

Fig. 3. Single-channel activity of rPanx1-EGFP and rPanx1S394D-EGFP over cell-attached and outside-out patches. (*A* and *B*) Representative cell-attached recordings from HeLa cells expressing rPanx1-EGFP (*A*) or rPanx1S394D-EGFP (*B*). Numbers shown at the left of current traces indicate applied potential to the patch pipette, V_p. (*C* and *D*) Representative outside-out recordings from HeLa cells expressing rPanx1-EGFP (*C*) or rPanx1S394D-EGFP (*D*) following membrane excision after achieving whole-cell mode. C, closed state; O, open-state amplitude for one channel; V_m, membrane potential. All-point amplitude histograms (counts) are shown on the right of current traces. (*E*) Single-channel (SC) current–voltage relationships from outside-out patches for rPanx1-EGFP in black (n = 8) and rPanx1S394D-EGFP in red (n = 5). (*F*) SC conductance–voltage relationships for rPanx1-EGFP in black and rPanx1S394D-EGFP in red calculated from data shown in *E*. In *E* and *F* all data points were fitted with a third-order linear regression. SC currents show inward rectification and predicted SC conductance is 45.5 pS at $V_m \approx 0$ mV.

density can only be stabilized by the neutralization of some R residues in the ring due to a shift in the negative base-10 logarithm of the acid dissociation constant (pK_a). R residues with a pK_a of 12 are always assumed to be positively charged. However, there are several examples where the pK_a of R residues could drop to 4 (*SI Appendix*, Fig. S8*B*), which allows these R residues at low dielectric constant to be sensitive to pH, and therefore some of the seven Rs of the ring could be in a neutral state (Arg0) to stabilize the electrostatic energy of the selectivity filter. To study the molecular properties of the selectivity filter interactions we used quantum mechanical methods based on the density functional theory at the ωB97XD97/6-31+G(d,p) level (41–43). Our calculations reflected clear differences in the value and orientation of the dipolar moment associated with both models; namely, for Arg+ the dipolar moment is equal to 53.8 D, pointing toward the intracellular region, allowing the translocation of Cl^-, whereas for Arg0 the dipolar moment is 15.6 D, pointing toward the extracellular region, allowing preferentially the translocation of cations to the extracellular region. To further characterize the nature of the attraction of the selectivity filter to anionic and cationic species, calculations of the passage of both Cl^- and K^+ along the central axis of the filter were performed. *SI Appendix*, Fig. S8*B*, shows that when cation (Arg)–π(Trp) interactions are present the filter tends to stabilize Cl^- by about 2.0 kcal/mol, compared to the anion located at the entry of the filter in the extracellular region, whereas for K^+ it is slightly higher in energy. In contrast, in the absence of a higher electrostatic polarization state at the filter, both Cl^- and K^+ are essentially predicted to be attracted by the pore. It should be noted that larger effects are obtained in the case of Arg+ due to enhancement by long-range polarization of the anion (Cl^-)–π(Trp) interactions, as compared to the case of less-electropositive states (i.e., Arg0). These results provide an insight that helps us to identify electronic mechanisms that modulate the passage of anionic and cationic species through the same selectivity filter.

Molecular Dynamics Simulations of the Phosphorylated State Reveal an Opening of the Lateral Tunnel That Promotes the Permeation of Anionic Species. To shed light on structural perturbations promoted by the phosphorylation of the S394 residue, we ran molecular dynamics (MD) simulation under equilibrium during 500 ns for the channel formed by rPanx1 or rPanx1S394Phos. At the same time, MD simulations were carried out using external electric fields of −100 mV and +100 mV for both rPanx1 and rPanx1-S394Phos channels. MD simulations revealed a systematic change in the organization of the selectivity filter when comparing rPanx1 to the rPanx1S394Phos channel. The filter of the rPanx1 channel maintains a rigid conformation such that the angle among W74 residues is stable during most of the MD trajectory. Instead, in the case of rPanx1S394Phos system, a more mobile W74 angle is observed. Therefore, we suggest that the phosphorylation of S394 increases the entropy of the selectivity filter compared to the rPanx1 channel. This evidence suggests that W74 residues are connected to S394 residues through an allosteric pathway, even though the distance between the S394 and the selectivity filter is more than ∼100 Å. Additionally, in both systems we observed the formation of lateral tunnels located in the water–membrane interface, delineated by lysine residues, as previously shown (5). Notoriously, in the rPanx1S394Phos channel this tunnel increases its volume by 700 $Å^3$ compared with the rPanx1 channel (*SI Appendix*, Fig. S9), which increases the probability that anionic species translocate through this route from the intracellular to the extracellular side.

We analyzed the electrostatic potential in rPanx1 and rPanx1-S394Phos channels (*SI Appendix*, Fig. S10 *A* and *B*). The changes of the lateral tunnel size and electrostatic potentials are depicted for the initial and final state of MD simulation for rPanx1-S394Phos channel (500 ns), where the increase of the size of a tunnel is clearly observed (*SI Appendix*, Fig. S10 *A* and *B*). We also obtained a longitudinal section of the electrostatic potential across the pore of rPanx1 and rPanx1S394Phos channels (*SI Appendix*, Fig. S10 *C* and *D*), revealing that in both channels the electrostatic potential at the level of the lateral tunnel becomes positive, which might enhance the translocation of anionic species, such as Cl^- and ATP. In the case of the rPanx1 channel, even though the lateral tunnel is smaller the protein appears more electropositive than in the rPanx1S394Phos channel. We suggest that the smaller size of the tunnel causes a low dielectric to propagate through the inner section of the channel. The same is depicted from a section parallel to the pore axis at the level of the tunnel, where the enhancement of the positive potential in rPanx1 appears clearly (*SI Appendix*, Fig. S10 *E* and *F*). On the other hand, the intracellular part of rPanx1S394Phos channel is noticeably more electronegative compared to rPanx1. The high negative potential at the intracellular side of the rPanx1S394Phos channel contrasted with the filter, which is more electropositive, is also depicted in *SI Appendix*, Fig. S11. These results suggest that ATP release via the main intracellular

entrance might be hampered in the phosphorylated channel and that an alternative route might be the lateral tunnels.

To corroborate this hypothesis, we performed an analysis using a steered MD (SMD) method to pull an ATP molecule from the intracellular side toward the inner cavity of rPanx1 through a lateral tunnel (Fig. 4 and Movie S1). After three replicas in each system, we extracted 50 configurations along the reaction coordinate of each SMD run to obtain the free energy of binding between the protein and the ATP molecule using the molecular mechanics generalized Born surface area (MM-GBSA) method. We observed that in the rPanx1 channel ATP does not enter through a lateral tunnel, due to a high steric hindrance. In contrast, in the rPanx1-S394Phos system the three replicas showed that ATP translocates through the cavity. The entry of ATP to the inner cavity ($\xi < 60$ Å) is promoted by the higher size of lateral tunnels, a ring of positive residues (Lys-306, Lys301, Lys211, Lys348, His-207), and a single cation bound to the ATP phosphates. With this information, we constructed a simplified free energy profile of the ATP pathway across a lateral tunnel. By comparing rPanx1 and rPanx1S394Phos profiles a flat energy landscape is observed in the case of rPanx1S394Phos, which represents a favorable translocation of ATP (Fig. 4*C*). Meanwhile, in the case of rPanx1, ATP gets stuck in the tunnel entry (60 Å $< \xi <$ 70 Å), as represented by a high-energy barrier in this zone, being less favorable for its translocation through the lateral tunnel. Those barriers might appear due to steric hindrance in the rPanx1 protein, whose lateral tunnel volume is reduced, as we showed before.

SMD simulations were then used in both systems to accelerate the passage of an ATP molecule (Fig. 4*B*) from the channel cavity toward the extracellular side. The free energy of binding between ATP and the protein was calculated using the MM-GBSA method, as described before. As seen from the rPanx1 inner cavity ($\xi = 60$ Å), an energy barrier of about 35 kcal/mol needs to be overcome by the ATP molecule before reaching the selectivity filter. The depth of the well in $\xi = 60$ Å shows that ATP binds more strongly than in the rPanx1 S394Phos channel, which may cause a slower diffusion across the rPanx1 protein. This strong interaction is mediated by the positive electrostatic potential in the cavity located at the level of lateral tunnels, and specifically by the residues Lys140, Lys26, and Lys373. Then, from $\xi = 30$ Å to $\xi = 0$, before reaching the extracellular side the ATP molecule diffuses through an energy landscape of similar magnitude between rPanx1 and rPanx1S394Phos, where the ATP molecule has to escape from the strong interaction with the selectivity filter ($\xi = 0$ Å) and neighbor residues. In the case of the rPanx1S394Phos channel the filter has more degrees of freedom compared to the wild type, which may facilitate that ATP escape to the extracellular side. Taken together, these results show that the rPanx1S394Phos shows higher volume of lateral tunnels and lower free energy profile along the pore of the channel, increasing the probability for ATP translocation from the intra- to the extracellular region.

We also inspected the translocation of a DAPI molecule through the pore of the Panx1 channel by running SMD. By observing the profiles obtained for rPanx1 and rPanx1S394Phos channels (*SI Appendix*, Fig. S12 and Movie S2) it is evidenced that rPanx1 protein profile displays increasing free energy values that make the translocation of DAPI molecules difficult, raising from 0, in the selectivity filter, to 15 kcal/mol in the inner cavity. Differently, in the rPanx1S394Phos channel a flat free energy profile is observed (from 0 to 5 kcal/mol), representing that the translocation of DAPI molecules is more favored, because the pore of the channel in the intracellular region has a more electronegative potential compared to the rPanx1. Moreover, we obtained the solvent-accessible surface area (SASA) of residues located in the intracellular section at the level of lateral tunnels. The SASA of those residues resulted to be higher in the rPanx1S394Phos channel compared to the rPanx1 channel (~2,200 Å^2 vs. ~2,000 Å^2, respectively). This value shows that in the rPanx1S394Phos protein those residues

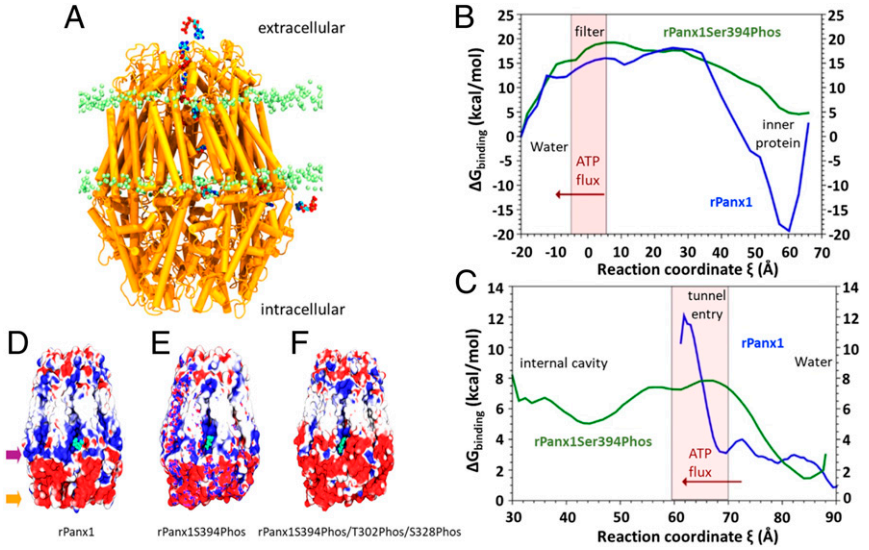

Fig. 4. Trajectory of intracellular ATP released to the extracellular space. (*A*) Trajectory of an ATP molecule (blue, cyan, and red) from the intracellular side through one lateral tunnel to the internal cavity, and from the cavity toward the extracellular side, in the upper part of the rPanx1 channel (represented in orange). Lipid heads are depicted in green. (*B*) MM-GBSA free energy profile for ATP obtained along the first pathway conducted with SMD (from the cavity at the level of the lateral tunnel [$\xi = +70$ Å] to the extracellular side of the protein [$\xi = -20$ Å]). The selectivity filter zone is represented as a pink bar. (*C*) MM-GBSA free energy profile for ATP obtained along the tunnel pathway conducted with SMD (from the water–lipid interface of the intracellular side [$\xi = +90$ Å] to the internal cavity of the channel [$\xi = +30$ Å]). The tunnel entry zone is depicted as a pink bar. In *B* and *C*, the red arrow indicates the direction of ATP movement. (*D* and *F*) Phosphorylation of three critical residues drastically changes the electrostatic potential of the lateral tunnel. Electrostatic potential of the channels phosphorylated by CaMKII and PKA. (*D*) rPanx1, (*E*) rPanx1S394Phos, site phosphorylated by CaMKII, (*F*) rPanx1S394Phos/T302Phos/S328Phos, two sites phosphorylated by PKA. Blue depicts electropositive zones, and negative potential areas are represented in red (scale bar from −1 kT/e to +1 kT/e). The ATP molecule appears in the lateral tunnel entry (in green). The purple arrow delineates the zone where S328 and T302 are located, and the orange arrow traces the area where S394 is situated.

are more available to interact with DAPI, favoring its translocation from the extra- to the intracellular side.

Additionally, we built a third system, introducing phosphate groups in T302 and S328 previously shown to be phosphorylated by PKA and maintain Panx1 channels insensitive to MS (40), in addition to S394. We obtained electrostatic potential maps of the three systems (rPanx1, rPanx1S394Phos, and rPanx1 S394Phos/T302Phos/S328Phos), and in the case of the triple phospho form of Panx1 the section of lateral tunnels became much more electronegative compared to the rPanx1 or rPanx1S394Phos (Fig. 4 *D*–*F*). Under these conditions ATP would encounter a strong electrostatic repulsion that makes its passage through lateral tunnels energetically unfavorable.

Discussion

In the present work we studied the molecular mechanism responsible for the increase in rPanx1 channel activity during MS stimulation. We found that rPanx1 channels expressed in HeLa cells are not intrinsically sensitive to MS, and its MS-dependent activation under physiological conditions involves an intracellular signaling cascade that begins with the activation of Piezo1 channels and submembrane increase in Ca^{2+} signal, followed by phosphorylation of the rPanx1 amino acid residue S394 by activated CaMKII. Our in silico studies suggest that this covalent modification expands the volume of lateral tunnels of the rPanx1 channel, allowing the release of ATP to the extracellular environment. These structural and allosteric modifications produce higher permeability for ATP and DAPI, without significant changes in single-channel conductance or outward rectification. All these modifications occurred in the absence of rPanx1 proteolysis and little, or no detectable, changes in the amount of fluorescent channels at the cell surface. The aforementioned signaling cascade may explain the release of ATP via rPanx1 channels expressed in various cell types and under different physiological conditions.

The increase in rPanx1 channel activity was dependent on the extracellular Ca^{2+} concentration, since it did not occur in cells bathed in saline solution without Ca^{2+} and was abrogated by intracellular BAPTA. Our results indicate that Piezo1 channels are responsible for the increase in Ca^{2+} signal upon MS stimulation, since application of Yoda1, an agonist of Piezo1, increases DAPI uptake rate in the absence of MS. The Yoda1-dependent increase in DAPI uptake was blocked by application of CBX and MS-induced increase in DAPI uptake was prevented by preincubation with a Piezo1 morpholino.

The submembrane increase in Ca^{2+} signal is likely to activate intracellular signaling molecules such as calmodulin and CaMKII. Preincubation with either W7 or KN62, inhibitors of calmodulin and CaMKII, respectively, also blocked the MS-dependent increase in DAPI uptake. We identified the amino acid residue S394 of rPanx1 as a putative phosphorylation site by CaMKII. Alanine substitution of residue S394 rendered an rPanx1 channel insensitive to MS, whereas the phosphomimetic mutation (S394D) yielded rPanx1 channels constitutively active. The latter was observed as elevated DAPI uptake and membrane currents in voltage clamp experiments under the cell-attached configuration only in HeLa cells transfected with rPanx1S394D-EGFP treated with suramin (probably preventing vesicular internalization of active channels). This observation was evaluated at the molecular level using MD simulations and free energy calculations, where the rPanx1S394Phos channel (the equivalent of the S394D mutant) showed a change in the electrostatic potential profile which contributes to a decrease in free energy barriers compared to rPanx1, which promotes the translocation of DAPI from the extracellular to the intracellular side.

Does EGFP affect the unitary conductance or activity of rPanx1 channels? Previous reports have shown that single-channel conductance for human or mouse Panx1 without tagged EGFP ranges from 12 or 20 pS at negative potentials and 80 or 95 pS at positive potentials, respectively (5, 44). Since our single-channel measurements were obtained from rPanx1-EGFP and range from 30 to 70 pS at negative and positive potentials, respectively, we cannot exclude the possibility that EGFP might affect unitary conductance, or whether the nature of rPanx1 differs from mouse or human orthologs. In addition, we replaced KCl with CsCl in our pipette recording solutions and included $BaCl_2$ in bath solution (to reduce noise), which was not used in the aforementioned studies.

As previously reported by others (10, 20, 44, 45), the Panx1 channels open and close at all voltages studied (−100 to +100 mV), but at least under resting conditions (between −10 and −20 mV) their permeability to ATP is likely to be very low because the DAPI (another small molecule) uptake rate was close to that detected in parental HeLa cells. Moreover, it can be speculated that a spontaneous active rPanx1 channel would allow release of ATP, reaching an extracellular concentration that could induce down-regulation of the molecular complex rPanx1 channel–P2 receptor (38). The possibility that activated purinergic P2 receptors might interact with rPanx1S394D promoting the internalization of this molecular complex is supported by our finding that internalization of rPanx1S394D-EGFP was prevented by suramin, a recognized blocker of P2 receptors (39).

Does phosphorylation affect the unitary conductance or the open probability of rPanx1 channels? In general, changes in unitary conductance of membrane channels are closely related to changes in channel permeability (46). In the present study, we found that phosphomimetic amino acid substitution of residue S394 by aspartate (D) does not significantly affect the unitary conductance of rPanx1-EGFP channels, supporting the hypothesis that changes in rPanx1 channel activity induced by CaMKII phosphorylation explain the increase in channel activity indicated by the increase in DAPI uptake rate. Notably, in voltage clamp experiments using the cell-attached configuration we detected more spontaneous unitary current events in cells transfected with rPanx1S394D-EGFP and an absence of unitary current in cells transfected with rPanx1-EGFP, suggesting that phosphorylation of S394 increases the open probability of rPanx1 channels. Nevertheless, this finding might not completely explain the increase in DAPI uptake rate, which reflects an increase in channel permeability. An alternative and more likely explanation could be that phosphorylation of S394 located in the C-terminal domain causes relevant allosteric and surface potential changes of the channel pore. In accordance with this possible explanation, our in silico studies revealed critical changes in the selectivity filter located in the vestibule of the pore located close to the extracellular domain of the channels, as well as changes in affinity of the permeant molecule to different domains of the channel pore due to changes in electronegativity of the molecular environment at the inner phase of the channel pore.

What can explain that under basal conditions Panx1 channels are preferentially permeable to Cl^- that is a monovalent negative ion but CaMKII phosphorylated rPanx1 channels are also permeable to positively (DAPI, +2) and negatively charged (ATP, −3) molecules? Certainly, the selectivity filter of rPanx1 presents an extraordinary interaction between Arg and Trp residues with an electronic configuration that allows the adaptation of this filter for anion and cation conduction, as was shown by quantum mechanics analysis. At the same time, our in silico studies show critical conformational changes induced by S394 phosphorylation. MD simulations revealed that the phosphorylation of the residue S394 generates an increase in lateral tunnel volume, as well as a decrease in the positive electrostatic potential of the pore, which all together decrease the energy barriers for the entry of ATP to the internal cavity via lateral tunnels. Electrostatic potential also showed that the inner section of rPanx1, near the lipid–water interface, has a strong positive potential that hinders the translocation of ATP toward the extracellular side, unlike the rPanx1S394Phos channel where the translocation is favored.

Previous studies have shown that Panx1 is a phosphoprotein, and increases in Panx1 channel activity have been associated with phosphorylation state changes of the protein subunit, either in threonine and/or serine (25) or tyrosine amino acid residues (40). We found that inhibition of the tyrosine Src family kinase with PP2 did not affect the increase in DAPI uptake induced by MS, favoring the role of CaMKII as discussed above. In addition, activation of Panx1 channels have been demonstrated under conditions that promote cell death (12, 36), which has been proposed to be mediated by elevated intracellular cytoplasmic Ca^{2+} concentration that activate proteases that cleave the C terminal of Panx1 (4, 12, 20). This mechanism of Panx1 channel activation is likely to be irreversible, which could be compatible with a feed-forward mechanism that leads to cell death. However, Panx1 is ubiquitously expressed in vertebrate cells and has been proposed to play numerous physiological roles. In favor of the existence of a different molecular mechanism that could explain a reversible activation of Panx1 channels, we propose that a transient increase in cytosolic Ca^{2+} activates calcineurin, which dephosphorylates the PKA sites and promotes phosphorylation of the CaMKII site of rPanx1, explaining the ATP release associated with reversible changes in cell responses. An example could be the rPanx1 channel-mediated ATP released from skeletal myofibers after repetitive contraction known to potentiate muscle contraction force (25). In favor of this possibility, we found that MS induced a transient increase in cytoplasmic Ca^{2+} signal that did not promote proteolysis of rPanx1 as revealed by Western blot analysis and the predicted conformational changes of phosphorylated rPanx1 channel that would favor ATP release via lateral tunnels. This response could be stopped by dephosphorylation of CaMKII or phosphorylation of rPanx1 channels by PKA, as predicted by our informatics analysis in which phosphorylation of the PKA sites previously shown to prevent the increase in rPanx1 channel activity induced by MS (40) also changes the electrostatic profile of the rPanx1 channel, hindering the ATP passage through lateral tunnels despite being phosphorylated in S394.

The inhibition mediated by PKA might partially explain the controversy on whether Panx1 channels are mechanosensitive or not (8). With regard to this issue, it is relevant to notice that the hPanx1 isoform does not present putative CaMKII phosphorylation sites including the amino acid residue S394 present in rPanx1, but it presents a putative PKA site (S329 instead of S328 present in rPanx1), which might inhibit hPanx1 channel activity and dephosphorylation through calcineurin and could explain the MS sensitivity of hPanx1 channel. Moreover, if the cell of interest presents a high intracellular cAMP concentration that activates PKA, the MS stimulation might be ineffective in promoting activation of rPanx1 channels. Under the same concept, if the cell type under study expresses very low or does not express calcineurin, the dephosphorylation of PKA sites might not occur, making the rPanx1 channel apparently insensitive to MS. In support of the latter, we described herein that HeLa hPanx1-mCherry cells treated with cyclosporine A, a calcineurin inhibitor, become insensitive to MS.

Materials and Methods

Reagents. CBX, lanthanum (III) chloride (La^{3+}), KN62, cyclosporine A (CsA), and PP2 were purchased from Sigma-Aldrich; DAPI and FURA–2 AM were purchased from Invitrogen, Dulbecco's modified Eagle's medium and RPMI 1640 were from Gibco, and Turbo Fect reagent was from Thermo Scientific. Yoda1 was from Tocris and W-7 was from Cayman Chemical. Rabbit anti-Panx1 previously described (25) was used.

Cells and Dye Uptake. Parental HeLa cells were obtained from the American Type Culture Collection and cultured as previously described (40). Non-transfected or transfected cells with different constructs as described below were MS-stimulated and dye uptake was evaluated as previously described (40). The dye uptake rates are shown as the average dye uptake divided by time ± SE, normalized to the baseline dye uptake rate.

Site-Directed Mutagenesis. Mutations were carried out using the Phusion Site-Directed Mutagenesis Kit, using as template DNA the plasmid pRK5 containing the insert of rPanx1 fused to EGFP (pRK5-rPanx1-EGFP) as described previously (40). *SI Appendix*, Table S1 shows DNA segments of the wild-type and mutant DNA constructs (second column) and protein sequences (third column). Mutated and original codons are highlighted in red boxes in the second column. Targeted serine (S) residues substituted by alanine (A) or aspartate (D) are highlighted in red in the third column. Mutations of the amino acid residues S384A, S394A, and S394D were made by using specific PCR primers containing the mutagenic sequence in the forward primer. *SI Appendix*, Table S2 shows the nucleotide sequence of forward and reverse PCR primers; the mutated codons are highlighted in bold. The previously described pRK5 vector that contains only the EGFP insert (empty vector) and the mutant rPanx1S394A-EGFP were used (40).

Determination of Intracellular Free Ca^{2+}. The intracellular Ca^{2+} signal was first evaluated with FURA-2 as described previously (16). In order to detect submembrane localized Ca^{2+} signals, HeLa cells grown on coverslips were transfected with a genetically encoded Ca^{2+} indicator protein pN-Lck-GCAMP3 plasmid (a generous gift from Baljit Khakh, Los Angeles, CA, Addgene plasmid no. 26974) as previously described (47). Cells were imaged 24 to 48 h post-transfection by TIRF microscopy using an inverted microscope (Eclipse Ti-E; Nikon) implemented with a 100× APO TIRF objective (numerical aperture 1.49; Nikon) and a Perfect Focus Unit TI-ND6-PFS (Nikon). The Lck-GCAMP3 transfected HeLa cells were illuminated with a 488-nm laser (OBIS 488-20LS; Coherent), and TIRF images were attained using a C11440 digital camera (ORCA-FLASH 2.0; Hamamatsu Photonics) together with the NIS-Elements Advanced Research 4.3 software (Nikon). MS consisted of the application of 6 mL recording solution dropped from 15 cm high as previously described (40), and images were obtained at 1-s intervals using stream mode. Stimulation was achieved in the presence of 3 mM Ca^{2+}, in absence of nominal Ca^{2+}, and in cells preloaded with 20 μM of the cell-permeant Ca^{2+} chelator BAPTA-AM (20-min preincubation). Experiments were performed at room temperature (21 to 25 °C). In order to determine the relative changes in the fluorescent signals obtained, an individual region of interest was done for every cell, and background was subtracted from each. Individual data were normalized using the F/F_0 ratio to express the relative changes in submembrane Ca^{2+} signals over time. Four coverslips from different cultures per condition, five cells per coverslip, were analyzed. Statistical comparisons were made using one-way ANOVA, followed by Bonferroni post hoc test.

Electrophysiology and Patch-Clamp Recordings. Electrophysiology experiments were performed in a modified Krebs–Ringer (MKR) solution containing (in millimolar) NaCl, 140; CsCl, 5.4; $CaCl_2$, 1.8; $MgCl_2$, 1; $BaCl_2$, 2; and Hepes, 5 (pH 7.4). Electrodes were filled with a pipette solution containing (in millimolar) CsCl, 130; NaAsp, 10; $CaCl_2$, 0.26; $MgCl_2$, 1; EGTA, 2; TEACl, 7; and Hepes, 5 (pH 7.2). Cells grown in coverslips were transferred to an experimental chamber mounted on an Olympus X-70 microscope and perfused with MKR solution at 30 °C. Briefly, a Multiclamp 200b amplifier was used to measure total and single channel currents with cell-attached, whole-cell, and outside-out patch-clamp techniques. We applied brief prepulses of −20 mV before each voltage step to measure macroscopic conductance and control stability between voltage steps. Recordings and data analysis were performed using P-clamp software (Axon Instruments) and Digidata 1322A (Axon Instruments). Measured currents were low-pass-filtered at 2 kHz and sampled at a rate of 50 to 100 μs.

Western Blot. rPanx1 was detected as described previously (25). In brief, HeLa transfectants or parental cells were stimulated as described for DAPI uptake experiments and rapidly were harvested using a rubber policeman on ice-cold saline solution. Then, cells were pelleted and homogenized. Samples were used to evaluate protein concentration, separation of protein in 8% sodium dodecyl sulfate polyacrylamide gels, and detection of Panx1 as described (25).

Confocal Immunofluorescence. HeLa cells seeded at 70% confluent onto 10-mm glass coverslips were transiently transfected (12 h) with rPanx1-EGFP or rPanx1S394D-EGFP, in the presence or absence of 100 μM suramin. Then, the cells were fixed with 4% paraformaldehyde for 10 min, washed four times with phosphate-buffered saline, and then mounted with Fluoromont G with DAPI. Confocal images were acquired on a confocal microscope (Nikon D-eclipse C1) at 100× oil objective; five stacks in the *z* axis, each 2 μm, were obtained. Fluorescence of Panx1-EGFP distribution was analyzed using NIS Elements control software (Nikon).

Energy Profile Using Quantum Chemical Calculations. Density functional theory all-electron single-point calculations at the WB97XD/6-31G(d,p) level of theory were performed on two models of the selectivity filter using the Gaussian 16 package of programs. The two models represent the selectivity filter under two extreme states, seven arginine residues with a positive charge and seven arginine residues under a neutral state. The evaluation of intermediate states with different numbers of arginine charges requires a significant effort, which is out of the scope of the present work. The WB97XD functional belongs to a class of long-range corrected hybrid density functionals that include atom–atom dispersion corrections. In fact, such a range-separated model properly incorporates both short-range and long-range interactions. Additionally, solvent effects (water) were considered in all calculations via the COSMO (c-PCM) model. The electrostatic potential was evaluated within the CHELPG approach (48). In the first model for the selectivity filter (Arg+) we have considered that each arginine branch bears a positive charge [i.e., $-CH_2$-NH-C+$(NH_2)_2$], whereas in the second one (Arg0) it has been made neutral [i.e., $-CH_2$-N = $C(NH_2)_2$].

Molecular Modeling and MD Simulations. A full model of the rPanx1 channel, sequence code Q96RD7 (UniProt), was built using the program Modeler (49). Wild-type human Panx1 channel cryogenic electron microscopy structure (Protein Data Bank ID code 6WBF) was used as a template. Given the lack of reference structures for loops formed by residues 163 to 190 and coils of residues 374 to 426, an ab initio model for the segments was done using the QUARK online server (50, 51). Then, the ab initio model of the missing residues was ensembled into the rPanx1 channel model structure. Additionally, in order to obtain a structure with S394Phos, the seven S394 residues were replaced for phosphoserine using the parameters reported by Craft and Legge (52), using tleap in AMBER20. The full model was then inserted into a phosphatidyloleoyl phosphatidylcholine bilayer membrane of 180 × 180 $Å^2$. Then, a water box (TIP3P model) was added and neutralized with a concentration of 0.15 mol/L KCl. The Amber19sb force field was used for proteins (53), LIPID 17 force field for lipids (54), the TIP3P water model (55), and ion parameters reported by Joung and Cheatham (56). ATP and DAPI molecules were parameterized using the GAFF force field (57) and the ANTECHAMBER (58) module of AMBER20 package. VMD software was used to build the systems (59). The system was then submitted to energy minimization and subsequent equilibration protocol by 500 ns under NPT ensemble at 310 K using AMBER 20 software (60, 61). Electrostatic interactions were computed using particle mesh Ewald under periodic boundary conditions. The velocity rescale (v-rescale) thermostat (59) was employed to maintain the temperature constant at 310 K. A semiisotropic Berendsen barostat (59) was used to keep the pressure at 1bar. After the equilibration, the system was subjected to an external electric field applied along the z axis to generate the desired voltage.

The voltage (V) was calculated as $V = ELz$, where E represents the applied electric field and LZ the length of the simulation box along the z axis, as reported previously (62, 63). Both systems rPanx1S394Phos and rPanx1 were subjected to +100 mV, 0 mV, and −100 mV, each for 500 ns.

An SMD method (64) was employed to sample the trajectory of ATP/DAPI molecules across the channel in an affordable calculation time. SMD calculation applies an external force on a dummy atom through a reaction coordinate. Three SMD sampling pathways were considered. The first pathway was designed to sample the route of the ATP from the inner cavity to the extracellular side. The reaction coordinate ξ was defined here as the center of mass distance between the ATP molecule and the seven alpha carbon atoms of the W74 residues located in the selectivity filter. The second pathway delineates the translocation of ATP from intracellular water through the lateral tunnel. In this case, the reaction coordinate ξ was defined as the center of mass distance between the ATP molecule and two alpha carbon atoms from residues located at the other end of the entry pathway (Ala-33 and Glu-19 of the next monomer), projected in the y axis. The third approach considered applying SMD to study the translocation of the DAPI molecule from the extracellular to the intracellular side along the entire pore, using the same reaction coordinate as in the first pathway. In all the cases, an external force of 1 Å/kcal*mol was used to pull the molecules. At least three replicates of 20 ns each one were performed in nonphosphorylated and S394Phos systems to sample the first and second pathways, while in the case of the third pathway eight replicates of 65 ns of each system were performed to obtain a reasonable free energy profile. In the case of the first and second approaches, the MM-GBSA method (65) was used over SMD trajectories to calculate the relative free energy of binding in each point of the reaction coordinate. Thus, in each frame the free energy of binding was calculated as follows:

$$\Delta G_{\text{binding}} = G_{\text{complex}} - \left(G_{\text{protein}} + G_{\text{ATP}}\right),$$

where

$$G = H_{\text{MM}} + G_{\text{solv}} - T\Delta S_{\text{conf}}.$$

The H_{MM} contribution corresponds to the sum of the terms calculated from MD simulations. Solvation free energy G_{solv} was obtained through the generalized Born approach and SASA. The conformational entropy was not included, because of the large computational cost and low prediction accuracy. Electrostatic potential maps were computed using APBS (66) and PDB2PQR (67) to obtain the input files.

Statistical Analysis. Significant differences between groups were determined using the GraphPad Prism 6 program using two-way ANOVA with a Tukey posttest to perform multiple comparisons. The differences were considered significant with $P < 0.05$ ($^*P < 0.05$, $^{**}P < 0.005$, and $^{***}P < 0.001$). The number of repetitions of each experiment is mentioned at the bottom of each figure.

Data Availability. All study data are included in the article and/or supporting information.

ACKNOWLEDGMENTS. We thank Teresa Vergara for her excellent technical assistance. Parts of the experimental data in this paper are from a thesis submitted in partial fulfillment of the requirements for the Doctorate in Biological Sciences (X.L.) in the Pontificia Universidad Católica de Chile. This research was partially funded by Fondo Nacional de Desarrollo Científico y Tecnológico grants 21140955 (to X.L.), 3180272 (to N.P.-P.), 1170733 (to F.D.G.-N.), 1191329 (to J.C.S. and Y.D.), 1171240 (to A.D.M.), 1181582 (to E.C.), and 11201113 (to Y.D.), as well as grant ICM-ANID, Project P09-022 from the Centro Interdisciplinario de Neurociencias de Valparaíso (to J.C.S., A.D.M., and F.D.G.-N.).

1. Y. Panchin *et al*., A ubiquitous family of putative gap junction molecules. *Curr. Biol.* **10**, R473–R474 (2000).
2. A. Baranova *et al*., The mammalian pannexin family is homologous to the invertebrate innexin gap junction proteins. *Genomics* **83**, 706–716 (2004).
3. Y.-H. Chiu, M. S. Schappe, B. N. Desai, D. A. Bayliss, Revisiting multimodal activation and channel properties of Pannexin 1. *J. Gen. Physiol.* **150**, 19–39 (2018).
4. G. Dahl, The Pannexin1 membrane channel: Distinct conformations and functions. *FEBS Lett.* **592**, 3201–3209 (2018).
5. Z. Ruan, I. J. Orozco, J. Du, W. Lü, Structures of human pannexin 1 reveal ion pathways and mechanism of gating. *Nature* **584**, 646–651 (2020).
6. W. Ma *et al*., Pannexin 1 forms an anion-selective channel. *Pflugers Arch.* **463**, 585–592 (2012).
7. R. A. Romanov *et al*., The ATP permeability of pannexin 1 channels in a heterologous system and in mammalian taste cells is dispensable. *J. Cell Sci.* **125**, 5514–5523 (2012).
8. L. Bao, S. Locovei, G. Dahl, Pannexin membrane channels are mechanosensitive conduits for ATP. *FEBS Lett.* **572**, 65–68 (2004).
9. S. Locovei, J. Wang, G. Dahl, Activation of pannexin 1 channels by ATP through P2Y receptors and by cytoplasmic calcium. *FEBS Lett.* **580**, 239–244 (2006).
10. P. Pelegrin, A. Surprenant, Pannexin-1 mediates large pore formation and interleukin-1beta release by the ATP-gated P2X7 receptor. *EMBO J.* **25**, 5071–5082 (2006).
11. G. A. Ransford *et al*., Pannexin 1 contributes to ATP release in airway epithelia. *Am. J. Respir. Cell Mol. Biol.* **41**, 525–534 (2009).
12. F. B. Chekeni *et al*., Pannexin 1 channels mediate 'find-me' signal release and membrane permeability during apoptosis. *Nature* **467**, 863–867 (2010).
13. M. Sridharan *et al*., Pannexin 1 is the conduit for low oxygen tension-induced ATP release from human erythrocytes. *Am. J. Physiol. Heart Circ. Physiol.* **299**, H1146–H1152 (2010).
14. S. O. Suadicani *et al*., ATP signaling is deficient in cultured Pannexin1-null mouse astrocytes. *Glia* **60**, 1106–1116 (2012).
15. K. Michalski *et al*., The Cryo-EM structure of pannexin 1 reveals unique motifs for ion selection and inhibition. *eLife* **9**, e54670 (2020).
16. P. A. Harcha *et al*., Hemichannels are required for amyloid β-peptide-induced degranulation and are activated in brain aast cells of APPswe/PS1dE9 mice. *J. Neurosci.* **35**, 9526–9538 (2015).
17. J. Wang, G. Dahl, Pannexin1: A multifunction and multiconductance and/or permeability membrane channel. *Am. J. Physiol. Cell Physiol.* **315**, C290–C299 (2018).
18. J. Wang, D. G. Jackson, G. Dahl, Cationic control of Panx1 channel function. *Am. J. Physiol. Cell Physiol.* **315**, C279–C289 (2018).
19. W. Ma, H. Hui, P. Pelegrin, A. Surprenant, Pharmacological characterization of pannexin-1 currents expressed in mammalian cells. *J. Pharmacol. Exp. Ther.* **328**, 409–418 (2009).
20. Y.-H. Chiu *et al*., A quantized mechanism for activation of pannexin channels. *Nat. Commun.* **8**, 14324 (2017).
21. R. J. Thompson, N. Zhou, B. A. MacVicar, Ischemia opens neuronal gap junction hemichannels. *Science* **312**, 924–927 (2006).

22. M.-C. Kienitz, K. Bender, R. Dermietzel, L. Pott, G. Zoidl, Pannexin 1 constitutes the large conductance cation channel of cardiac myocytes. *J. Biol. Chem.* **286**, 290–298 (2011).
23. T. Woehrle *et al*., Pannexin-1 hemichannel-mediated ATP release together with P2X1 and P2X4 receptors regulate T-cell activation at the immune synapse. *Blood* **116**, 3475–3484 (2010).
24. A. Chandrasekhar, A. K. Bera, Hemichannels: Permeants and their effect on development, physiology and death. *Cell Biochem. Funct.* **30**, 89–100 (2012).
25. M. A. Riquelme *et al*., The ATP required for potentiation of skeletal muscle contraction is released via pannexin hemichannels. *Neuropharmacology* **75**, 594–603 (2013).
26. J. P. Reyes, C. Y. Hernández-Carballo, G. Pérez-Flores, P. Pérez-Cornejo, J. Arreola, Lack of coupling between membrane stretching and pannexin-1 hemichannels. *Biochem. Biophys. Res. Commun.* **380**, 50–53 (2009).
27. T. Miyamoto *et al*., Functional role for Piezo1 in stretch-evoked Ca^{2+} influx and ATP release in urothelial cell cultures. *J. Biol. Chem.* **289**, 16565–16575 (2014).
28. S. Wang *et al*., Endothelial cation channel PIEZO1 controls blood pressure by mediating flow-induced ATP release. *J. Clin. Invest.* **126**, 4527–4536 (2016).
29. F. Sachs, Stretch-activated ion channels: What are they? *Physiology (Bethesda)* **25**, 50–56 (2010).
30. R. G. Johnson *et al*., Connexin hemichannels: Methods for dye uptake and leakage. *J. Membr. Biol.* **249**, 713–741 (2016).
31. O. P. Hamill, B. Martinac, Molecular basis of mechanotransduction in living cells. *Physiol. Rev.* **81**, 685–740 (2001).
32. A. V. Staruschenko, A. V. Sudarikova, Y. A. Negulyaev, E. A. Morachevskaya, Magnesium permeation through mechanosensitive channels: Single-current measurements. *Cell Res.* **16**, 723–730 (2006).
33. R. Syeda *et al*., Chemical activation of the mechanotransduction channel Piezo1. *eLife* **4**, e07369 (2015).
34. M. T. Swulius, M. N. Waxham, Ca(2+)/calmodulin-dependent protein kinases. *Cell. Mol. Life Sci.* **65**, 2637–2657 (2008).
35. J. Rumi-Masante *et al*., Structural basis for activation of calcineurin by calmodulin. *J. Mol. Biol.* **415**, 307–317 (2012).
36. N. L. Weilinger, P. L. Tang, R. J. Thompson, Anoxia-induced NMDA receptor activation opens pannexin channels via Src family kinases. *J. Neurosci.* **32**, 12579–12588 (2012).
37. A. W. Lohman *et al*., Pannexin 1 channels regulate leukocyte emigration through the venous endothelium during acute inflammation. *Nat. Commun.* **6**, 7965 (2015).
38. A. K. J. Boyce, M. S. Kim, L. E. Wicki-Stordeur, L. A. Swayne, ATP stimulates pannexin 1 internalization to endosomal compartments. *Biochem. J.* **470**, 319–330 (2015).
39. P. M. Dunn, A. G. Blakeley, Suramin: A reversible P2-purinoceptor antagonist in the mouse vas deferens. *Br. J. Pharmacol.* **93**, 243–245 (1988).
40. X. López *et al*., Stretch-induced activation of Pannexin 1 channels can be prevented by PKA-dependent phosphorylation. *Int. J. Mol. Sci.* **21**, 9180 (2020).
41. S. Grimme, Semiempirical GGA-type density functional constructed with a long-range dispersion correction. *J. Comput. Chem.* **27**, 1787–1799 (2006).
42. S. Grimme, J. Antony, S. Ehrlich, H. Krieg, A consistent and accurate ab initio parametrization of density functional dispersion correction (DFT-D) for the 94 elements H-Pu. *J. Chem. Phys.* **132**, 154104 (2010).
43. S. Grimme, S. Ehrlich, L. Goerigk, Effect of the damping function in dispersion corrected density functional theory. *J. Comput. Chem.* **32**, 1456–1465 (2011).
44. T. Nomura *et al*., Current-direction/amplitude-dependent single channel gating kinetics of mouse pannexin 1 channel: A new concept for gating kinetics. *Sci. Rep.* **7**, 10512 (2017).
45. R. Bruzzone, S. G. Hormuzdi, M. T. Barbe, A. Herb, H. Monyer, Pannexins, a family of gap junction proteins expressed in brain. *Proc. Natl. Acad. Sci. U.S.A.* **100**, 13644–13649 (2003).
46. N. Palacios-Prado, F. F. Bukauskas, Modulation of metabolic communication through gap junction channels by transjunctional voltage; synergistic and antagonistic effects of gating and ionophoresis. *Biochim. Biophys. Acta* **1818**, 1884–1894 (2012).
47. M. C. Maldifassi *et al*., The interplay between α7 nicotinic acetylcholine receptors, pannexin-1 channels and P2X7 receptors elicit exocytosis in chromaffin cells. *J. Neurochem.* **157**, 1789–1808 (2020).
48. C. N. Breneman, K. B. Wiberg, Determining atom-centered monopoles from molecular electrostatic potentials. The need for high sampling density in formamide conformational analysis. *J. Comput. Chem.* **11**, 361–373 (1990).
49. A. Sali, T. L. Blundell, Comparative protein modelling by satisfaction of spatial restraints. *J. Mol. Biol.* **234**, 779–815 (1993).
50. Y. Zhang, Interplay of I-TASSER and QUARK for template-based and ab initio protein structure prediction in CASP10. *Proteins* **82** (suppl. 2), 175–187 (2014).
51. W. Zhang *et al*., Integration of QUARK and I-TASSER for Ab initio protein structure prediction in CASP11. *Proteins* **84** (suppl. 1), 76–86 (2016).
52. J. W. J. Craft, Jr, G. B. Legge, An AMBER/DYANA/MOLMOL phosphorylated amino acid library set and incorporation into NMR structure calculations. *J. Biomol. NMR* **33**, 15–24 (2005).
53. C. Tian *et al*., ff19SB: Amino-acid-specific protein backbone parameters trained against quantum mechanics energy surfaces in solution. *J. Chem. Theory Comput.* **16**, 528–552 (2020).
54. C. J. Dickson *et al*., Lipid14: The amber lipid force field. *J. Chem. Theory Comput.* **10**, 865–879 (2014).
55. W. L. Jorgensen, J. Chandrasekhar, J. D. Madura, R. W. Impey, M. L. Klein, Comparison of simple potential functions for simulating liquid water. *J. Chem. Phys.* **79**, 926–935 (1983).
56. I. S. Joung, T. E. Cheatham III, Determination of alkali and halide monovalent ion parameters for use in explicitly solvated biomolecular simulations. *J. Phys. Chem. B* **112**, 9020–9041 (2008).
57. J. Wang, R. M. Wolf, J. W. Caldwell, P. A. Kollman, D. A. Case, Development and testing of a general amber force field. *J. Comput. Chem.* **25**, 1157–1174 (2004).
58. J. Wang, W. Wang, P. A. Kollman, D. A. Case, Automatic atom type and bond type perception in molecular mechanical calculations. *J. Mol. Graph. Model.* **25**, 247–260 (2006).
59. W. Kopec, B. S. Rothberg, B. L. de Groot, Molecular mechanism of a potassium channel gating through activation gate-selectivity filter coupling. *Nat. Commun.* **10**, 5366 (2019).
60. D. A. Case *et al*., The Amber biomolecular simulation programs. *J. Comput. Chem.* **26**, 1668–1688 (2005).
61. J. A. Maier *et al*., ff14SB: Improving the accuracy of protein side chain and backbone parameters from ff99SB. *J. Chem. Theory Comput.* **11**, 3696–3713 (2015).
62. B. Roux, The membrane potential and its representation by a constant electric field in computer simulations. *Biophys. J.* **95**, 4205–4216 (2008).
63. J. Gumbart, F. Khalili-Araghi, M. Sotomayor, B. Roux, Constant electric field simulations of the membrane potential illustrated with simple systems. *Biochim. Biophys. Acta* **1818**, 294–302 (2012).
64. S. Izrailev, A. R. Crofts, E. A. Berry, K. Schulten, Steered molecular dynamics simulation of the Rieske subunit motion in the cytochrome bc(1) complex. *Biophys. J.* **77**, 1753–1768 (1999).
65. H. Gohlke, D. A. Case, Converging free energy estimates: MM-PB(GB)SA studies on the protein-protein complex Ras-Raf. *J. Comput. Chem.* **25**, 238–250 (2004).
66. N. A. Baker, D. Sept, S. Joseph, M. J. Holst, J. A. McCammon, Electrostatics of nanosystems: Application to microtubules and the ribosome. *Proc. Natl. Acad. Sci. U.S.A.* **98**, 10037–10041 (2001).
67. T. J. Dolinsky, J. E. Nielsen, J. A. McCammon, N. A. Baker, PDB2PQR: An automated pipeline for the setup of Poisson-Boltzmann electrostatics calculations. *Nucleic Acids Res.* **32**, W665–W667 (2004).